Author/s:
Xu, M;Harley, WS;Ma, Z;Lee, PVS;Collins, DJ

Title:
Sound-Speed Modifying Acoustic Metasurfaces for Acoustic Holography

Date:
2023-04-06

Citation:
Xu, M., Harley, W. S., Ma, Z., Lee, P. V. S. & Collins, D. J. (2023). Sound-Speed Modifying Acoustic Metasurfaces for Acoustic Holography. Advanced Materials, 35 (14), https://doi.org/10.1002/adma.202208002.

Persistent Link:
https://hdl.handle.net/11343/332174

ADVANCED MATERIALS
www.advmat.de

Sound-Speed Modifying Acoustic Metasurfaces for Acoustic Holography

*Mingxin Xu, William S. Harley, Zhichao Ma, Peter V. S. Lee, and David J. Collins**

Acoustic metasurfaces offer unique capabilities to steer and direct acoustic fields, though these are generally composed of complex 3D structures, complicating their fabrication and applicability to higher frequencies. Here, an ultrathin metasurface approach is demonstrated, wherein planarized micropillars in a discretized phase array are utilized. This subwavelength metasurface is easily produced via a single-step etching process and is suitable for megahertz-scale applications. The flexibility of this approach is further demonstrated in the production of complex acoustic patterns via acoustic holography. This metasurface approach, with models used to predict their behavior, has broad potential in applications where robust, high-frequency acoustic manipulation is required, including microfluidics, cell/tissue engineering, and medical ultrasound.

1. Introduction

Metamaterials consist of artificial subwavelength structures and offer unique wave modulation capabilities to control wavefronts in a manner distinct from natural materials.[1–11] Metasurfaces are arrayed planar metamaterials capable of modulating wavefronts passing through them, and have found utility in physics and engineering applications for optical waves,[12,13] acoustic waves,[14–17] and elastic waves.[18,19] Acoustic metasurfaces in particular have been the focus of recent research,[20,21] with demonstrations of acoustic cloaking,[22–25] selective absorption,[26–28] focusing,[29–34] reflected wavefront manipulation,[35–38] passive phased array,[39] and acoustic holography.[40–42] These applications are generally realized by arraying metasurface units across an interface, resulting in spatially defined phase and/or amplitude modulation.[43–47] Functional acoustic metasurface subunits include those based on spiral structures,[48–51] Helmholtz resonators,[32,52–54] and hybrid resonance units,[3,55,56] which are designed to alter the propagation path length, thus changing the equivalent phase, and/or modify the amplitude of the transmitted wave at a given frequency. These passive acoustic metasurfaces, which are composed of units with 3D coiled or cavity structures,[57,58] have demonstrated great potential for acoustic wave manipulation. However, such structures show limited compatibility with conventional microfabrication processes,[59,60] which makes their application to high-frequency micromanipulation especially challenging.[20,61–68]

In this work, we demonstrate an acoustic metasurface in which subwavelength micropillars are used to achieve wavefront manipulation by modifying the effective density, and therefore sound speed, via a single-material, single-fabrication-step structure. Here the phase change is a function of the micropillar density in discretized subunits, where the micropillar height is uniform across the interface. Compared to other approaches, our acoustic metasurface demonstrates wavefront modulation using structures that can be fabricated using common silicon microfabrication techniques, making this particularly suitable for applications in miniaturized and planarized devices. Analytical and simulation models are further developed to predict the phase as a function of micropillar seeding density. We demonstrate the flexibility of this approach using the principles of acoustic holography, whereby a unique phase map results in an arbitrarily defined amplitude distribution at a target plane, and where the phase-encoding metasurface hologram pillars are 260 μm high at an operational frequency of 6.9 MHz, evidencing the smaller dimensions and high frequencies for which this metasurface approach is suited.[69–71] Compared with prior acoustic holography efforts, this acoustic metasurface realizes ultrathin and planar holographic kinoforms without the need for multilevel 3D fabrication. This is based on a novel approach and physical mechanism that extends the potential applications of acoustic holograms, and acoustic wavefront modulation generally, especially for high-frequency/small-wavelength

M. Xu, W. S. Harley, P. V. S. Lee, D. J. Collins
Department of Biomedical Engineering
University of Melbourne
Melbourne, Victoria 3010, Australia
E-mail: david.collins@unimelb.edu.au

Z. Ma
School of Biomedical Engineering
Shanghai Jiao Tong University
Shanghai, 200240, China

Z. Ma
Institute of Medical Robotics
Shanghai Jiao Tong University
Shanghai, 200240, China

D. J. Collins
Graeme Clarke Institute
University of Melbourne
Parkville, Victoria 3052, Australia

The ORCID identification number(s) for the author(s) of this article can be found under https://doi.org/10.1002/adma.202208002.

DOI: 10.1002/adma.202208002

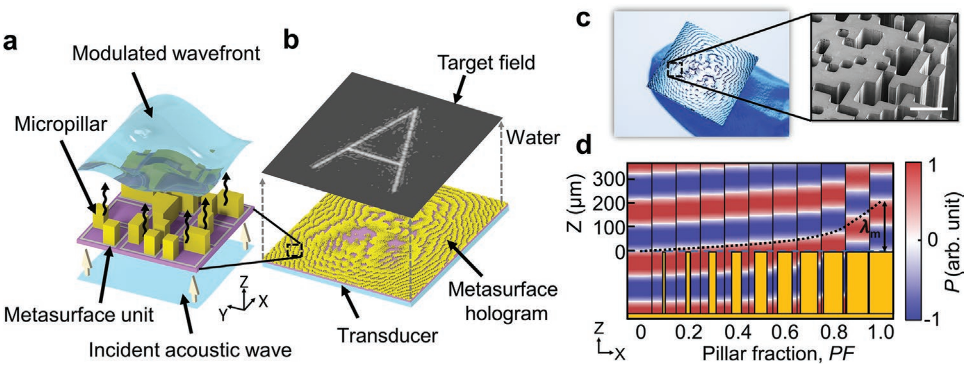

Figure 1. Sound-speed modifying pillar-based metasurfaces. a) Schematic of working principle where a metasurface, composed of metasurface units containing different pillar fractions, produces a modulated wavefronts from an incident acoustic wave. b) Example application in acoustic holography, where an acoustic hologram consisting of tens of thousands of metasurface units generates the target acoustic field at the target plane in water. c) Fabricated silicon-based metasurface hologram (1.5 cm × 1.5 cm) and helium-ion microscopy image showing the micropillars. Scale bar: 100 µm. d) The phase increases as pillar volume fraction (PF) increases.

micromanipulation. The design of simple, planar, and reproducible metasurfaces as demonstrated here accordingly expands the application of wavefront modulation techniques in microscale applications including microfluidics, cell/tissue engineering, and medical ultrasound.

2. Principles and Design

Figure 1a illustrates the sound-speed modifying acoustic metasurface concept. A modulated wavefront is generated by modifying the phase of the acoustic wave that is transmitted through the metasurface. Each metasurface unit is composed of a number of micropillars, where the phase shift in each metasurface unit is determined according to the micropillar volume fraction. Figure 1b demonstrates an example application of this metasurface for acoustic holography. Here an acoustic transducer generates incident acoustic waves, which transmit through the metasurface hologram plane. The wavefronts are then phase-modulated and propagate toward the target plane, resulting in the desired acoustic field. The fabricated all-silicon metasurface hologram (held on a finger for scale) and an inset helium ion microscopy image are shown in Figure 1c. In our implementation, the metasurface structures comprise 1.5 cm squares, each of which contains 150 × 150 metasurface units, and where each unit comprises 3 × 3 pixels, in which each pixel can be either etched or a pillar, resulting in nine discrete phase levels. Figure 1d shows the wavefronts corresponding to various pillar volume fractions (PF), where PF = W_p/W_u, in which W_p and W_u are the width of the metasurface and the unit, respectively; a PF of 0 corresponds to no pillar, a PF of 50% corresponds to a pillar one half of the domain width, and PF of 1 corresponds to 100% pillar infill. Notably, as this examines the case where the in-plane domain in question is subwavelength, an equivalent phase is produced regardless of the location or distribution of these pillars, so long as the total fraction of the cross-sectional area composed of pillar material remains the same. P in the color bar in Figure 1d is the acoustic pressure. Here, for PF = 0 (no pillar unit), the position where the acoustic pressure is zero for a given time step is at $Z = 0$. The pressure node subsequently moves along the wave propagation direction as PF increases (black dashed line), and the corresponding sound speed increases with increasing silicon (and decreasing water) makeup, resulting in an increased phase.

To implement this principle across a 2D metasurface, the metasurface plane is discretized into units, each comprising spaces in which pillar (or lack thereof) is placed. The phase of a unit is a function of PF, where the volume fraction of the pillar is the sum of pillars in a unit. Metasurface units are accordingly composed of same-height micropillars and surrounding water, as shown in **Figure 2**a, where the height and width of the metasurface pillars correspond to H_p and W_p, respectively. To produce a phase shift from 0 to 2π when the PF varies between 0 and 1, the height (H_p) of the metasurface is defined such that the waves in the micropillars and the waves in the water at the top of the metasurface are always in constructive interference, as shown in Figure 2a. Therefore, H_p is given by

$$H_p = \frac{1}{\frac{f}{c_m} - \frac{f}{c_p}} \tag{1}$$

where c_m and c_p are the longitudinal acoustic velocity of medium and micropillar, respectively, and f is the input

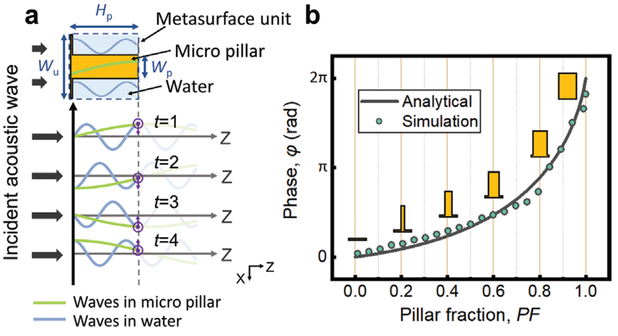

Figure 2. Pillar-based metasurface design principles. a) The waves in the micropillar and the water result in constructive interference at the top of a metasurface unit with $Z = H_p$. b) The relationship between pillar fraction and resulting phase, with analytical and simulation results shown.

frequency of the transducer (see the Supporting Information for derivation). As a lower H_p is desirable for fabrication, lowering the required etch depth and aspect ratio, this can be achieved by using materials with high c_p, according to Equation (1). In this work, silicon ($c_p \approx 8433$ m s^{-1}) is used to fabricate the metasurface micropillars due to its high c_p and ready compatibility with standard microfabrication etching processes.

To understand the relationship between PF and phase, the micropillars and surrounding water in a single unit are treated as fluid–solid composites.[72,73] The relationship between the effective acoustic velocity of the unit (c_{unit}) and the phase (φ) is expressed as (see the Supporting Information for calculation of c_{unit} and their derivations)

$$\varphi = 2\pi f H_p \left(\frac{1}{c_m} - \frac{1}{c_{unit}} \right) \tag{2}$$

where the relationship between PF and phase according to Equation (2) and simulation (see Figure S3 in the Supporting Information for details) is shown in Figure 2b. The results in this figure show that the metasurface achieves a continuous phase change from 0 to 2π within a PF range of 0–1 with low coefficient of variation ($< 10^{-3}$) of the resulting wavefronts.

To further demonstrate the relationship between the metasurface acoustic properties, frequency, and H_p, **Figure 3**a shows the critical dependence of H_p on frequency and the solid–liquid acoustic velocity ratio, where the medium used in this work is water ($c_m \approx 1480$ m s^{-1}). Qualitatively, these results indicate that when the ratio of c_p to c_m is less than 4 ($k \lesssim 4$), the pillar height is significantly larger than that when $k \gtrsim 4$, where the required pillar height asymptotes for higher solid sound speeds, thus reducing the dependence of H_p on k. Importantly, this further shows that H_p is inversely correlated with frequency f, indicating that thinner metasurface heights are required for increased frequencies, resulting in lower pillar height while retaining similar pillar aspect ratios in fabricated devices. Therefore, such metasurfaces are particularly suitable for high-frequency (>5 MHz) applications, where silicon pillars with corresponding heights of <300 µm can readily be fabricated using deep-reactive ion silicon etching.

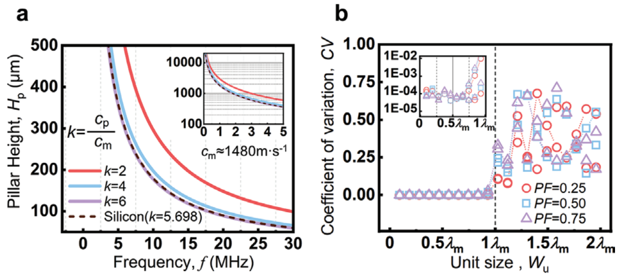

Figure 3. Impact of frequency and pillar dimensions. a) The pillar height decreases as the frequency increases and the acoustic velocity of the metasurface increases. For $k \gtrsim 4$(the ratio of pillar to fluid sound speeds), the dependence of pillar height on k is reduced and a lower pillar height is required. b) The relationship between the unit size and the coefficient of variation of the resulting wavefront, where subwavelength unit dimensions are required for effective wavefront control.

Figure 3b demonstrates the relationship between the unit size of the pillar array (W_u) and the wavefront coefficient of variation (CV), where CV = σ/μ, and σ and μ are the standard deviation and averaged pressure across a plane, respectively. Here a CV is calculated at planes 300 and 600 µm from the metasurface (as depicted in Figure S4 in the Supporting Information), thus with two CV measurements for each PF. This shows that an increased CV indicates the formation of nonuniform acoustic wavefronts and therefore a breakdown in the utility of this metasurface approach, which necessitates sufficiently small feature widths such that the silicon–water composite is effectively a single material from the perspective of the transmitted wavefront. For $W_u < 0.7\lambda_m$, the CV is in the order of 10^{-4}, where λ_m is the wavelength in the fluid medium, indicating desirable negligible wavefront deformation for subwavelength unit sizes. For larger unit sizes with $W_u \gtrsim \lambda_m$, the increased CV indicates that diffraction effects in the metasurface unit becomes significant.

To further improve the quality of wavefront, the concept of nonlocal metasurfaces has recently been proposed for generating accurate acoustic fields, in which the coupling between metasurface units has been taken into account.[74] Here, solid/fluid–mechanical coupling via local evanescent fields and within the solid elements themselves can impact the uniformity of the acoustic field in the far field in structures that especially subject to these effects and can take advantage of this. Accordingly, design methods for nonlocal acoustic metasurfaces including coupled structures[74–76] and deep learning[77] have been reported. Our structures, however, incorporate relatively simple longitudinal elements, and while a local evanescent field evolves at pillar extrema (as shown in Figure S5 in the Supporting Information), this does not impact the acoustic field in the far-field, and where simulation results incorporate solid-mechanical coupling effects without strong evidence for the impact of evanescent fields and mechanical coupling through the metasurface structures. Nevertheless, discontinuities in the phase of adjoining metasurface domains requires a nonzero length over which acoustic wavefronts evolve in the fluid, where the local acoustic field directly above this discontinuity is a summation of the contributions from both phase domains. Figure S6 (Supporting Information) examines the effect of phase difference between adjacent regions on the resulting coupling length, where these lengths increase with phase differentials, although only up to the scale of the metasurface depth itself.

3. Experiments

Acoustic holograms[71,78–80] are an excellent test of the achievable complexity and flexibility of this approach, where acoustic holography results in a designed acoustic wavefield at a target plane. The generation of a metasurface-based acoustic hologram is shown in **Figure 4**. To generate an acoustic hologram, first the desired input image (i.e., the target acoustic pressure field) is defined, where the binary amplitude of the letter "A" is located in a rectangular domain of 1.5 cm × 1.5 cm (Figure 4a–f). The iterative angular spectrum approach (IASA),[71,81] described in detail in the Experimental Section, is then used to calculate

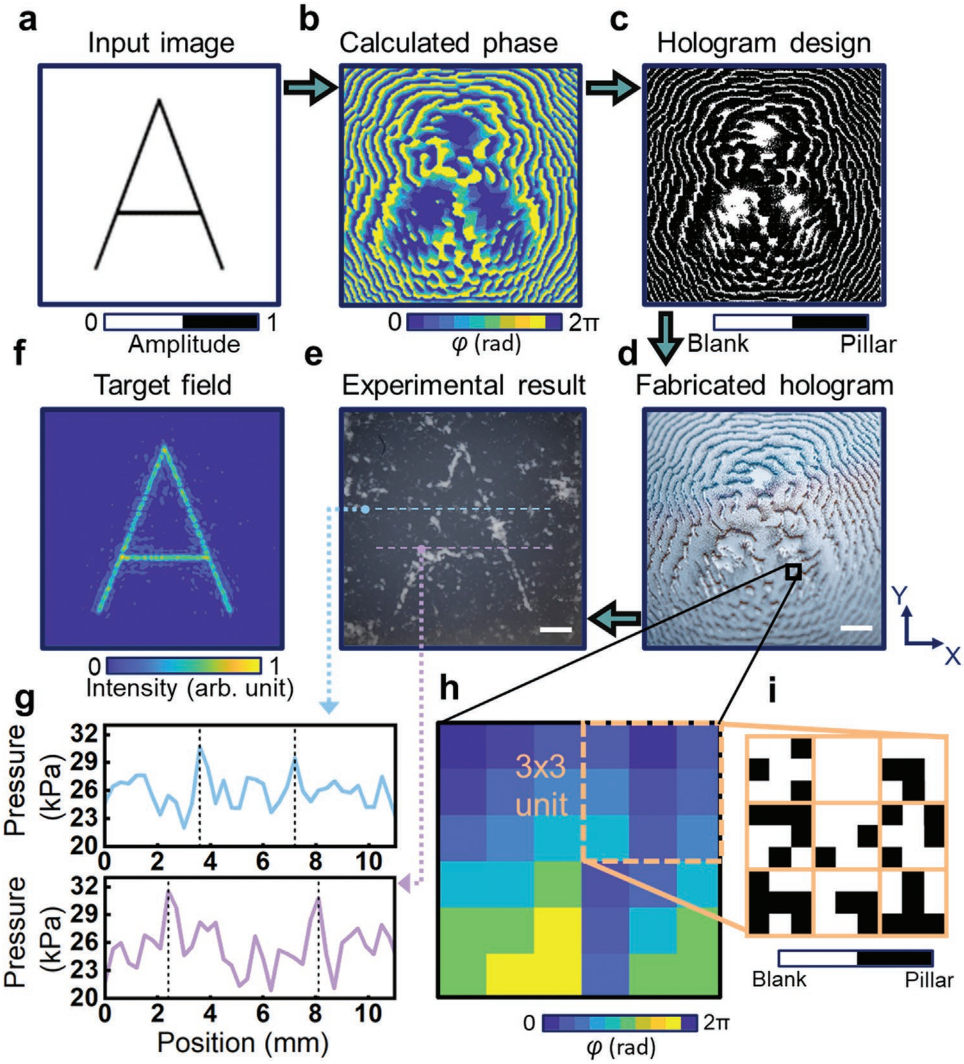

Figure 4. Metasurface-based acoustic holography. a) Input image with a binary amplitude. b) Phase map calculated from the input image. c) The hologram design transformed by the phase map that defines the micropillar positioning. d) Fabricated hologram. e) Experimental PDMS microparticle patterning. f) Target field output from IASA calculations. g) Hydrophone scans of pattern cross-sections of (e). h) A localized phase map. i) A subset of 3 × 3 = 9 units is displayed, where each unit contains 9 pixels, and each pixel represents either a pillar or blank position. The unit size is 100 µm × 100 µm and scale bars are 2 mm.

the phase map (Figure 4b) of the acoustic hologram. Here each metasurface unit has 9 pixels, and each pixel can be either a pillar or cavity (i.e., composed of water or silicon), yielding 9 discrete phase levels. To utilize the IASA with these discrete phase levels, the phase of each holographic element is converted to the closest phase distribution at each step of the iteration (as per Equation (2)).

The metasurface-based holograms are then designed (Figure 4c) and fabricated (Figure 4d) via silicon etching, where 22 500 metasurface units are produced on a single hologram with a pillar height of 260 ± 20 µm. We randomize the position of pillar elements within each unit to reduce the potential for off-target in-plane resonances (those occurring along the plane of the metasurface) to occur, where periodic features have the potential to generate resonances at frequencies corresponding to a given periodicity. While the magnitude of such resonances arising from subwavelength features would be small, and where this not a criterion for the viability of this metasurface approach, randomizing the positioning of pillars within units minimizes the potential for unintended periodicity to occur in any direction in the metasurface plane across the variety of arbitrary metasurface phase maps that might be produced. The specific position of a pillar in a given 9 pixel unit is thus randomly assigned, where Figure S7 (Supporting Information) shows that different randomized micropillar positions in a metasurface unit do not impact the resulting phase. Figure S8 (Supporting Information) also shows the bandwidth for the hologram of letter "A" designed at 6.9 MHz, where the peak signal-to-noise ratio is used to describe the target plane quality at different frequencies and is greater than 19 dB in the ±0.3 MHz bandwidth of the design frequency.

The 6.9 MHz acoustic waves are generated by a lithium niobate ($LiNbO_3$) transducer, with wavefronts passing through the phase-modulating metasurface. The target acoustic field is

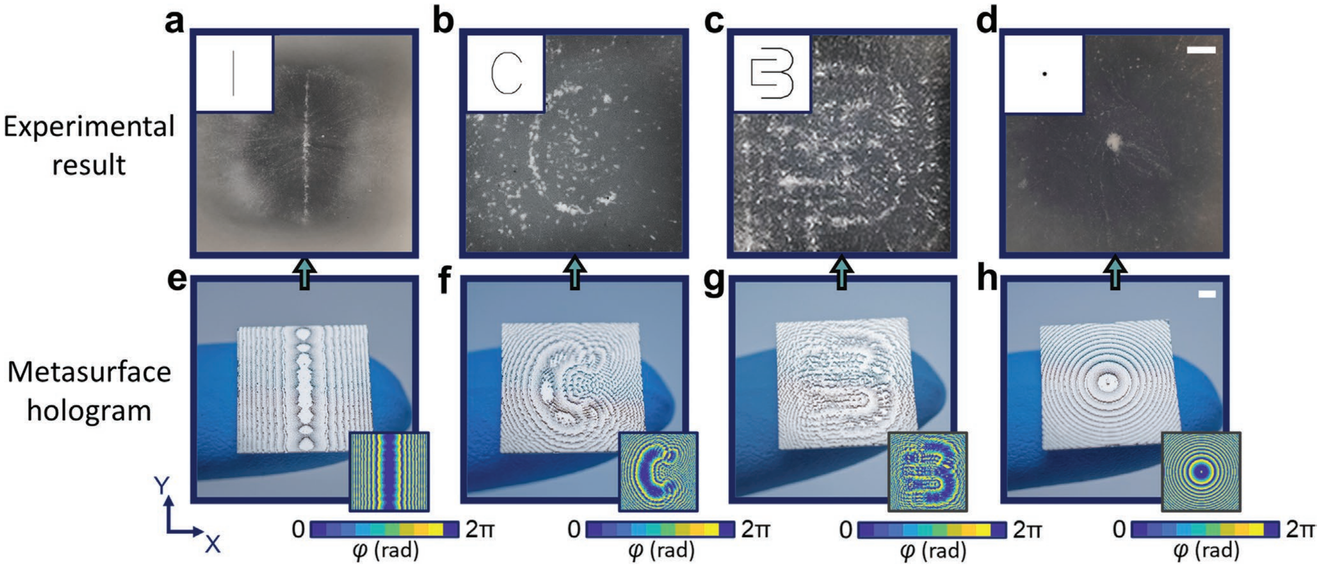

Figure 5. Metasurface-based hologram particle patterning, for example, numbers, letters, and shapes. a) Number "1." b) Letter "C." c) Logo of the Collins Biomicrosystems Laboratory. d) Focus point for particle aggregation. e–h) The corresponding metasurface-based holograms, where insets show the phase distribution. Scale bars: 2 mm.

defined at a distance of 1.3 cm from the metasurface, where poly(dimethylsiloxane) (PDMS) particles are used to visualize the field and hydrophone scans are implemented to characterize the target acoustic pressure field (Figure 4g). The preparation and experimental procedures are detailed in the Experimental Section, and PDMS microparticle patterning is shown in Video S1 (Supporting Information).

Microparticles can be assembled into arbitrarily defined target patterns using this approach. **Figure 5** demonstrates its flexibility in defining the contours of a number- (Figure 5a), letter- (Figure 5b), shape- (Figure 5c, logo of Collins Biomicrosystems Laboratory), and point-based particle aggregation (Figure 5d). The hologram fabrication results and phase distribution corresponding to Figure 5a–d, respectively, are shown in Figure 5e–h. Figure S9 (Supporting Information) shows the measurement of phase delay for a cross-section in Figure 5e, demonstrating good agreement between the designed and experimentally measured phase. Note, however, that a finite-width hydrophone, whose width is on the order of the unit dimensions, has the effect of spatially averaging the observed phase delays.

4. Conclusion

We report an acoustic metasurface that employs planar micropillars for robust wavefront modulation. The micropillar volume fraction of single subwavelength units determines the effective sound speed and thus the corresponding phase of each unit, where each unit can be treated as an independent acoustic point source. The planarized structures are comparatively straightforward to fabricate compared to the complex 3D and printed structures required in previous work, where we instead utilize a single-layer, single-step etching process, making this far more amenable to smaller structures, and correspondingly higher frequencies, than approaches requiring 3D printing. In this work, we further demonstrate the theoretical basis of this pillar-based metasurface, showing that the pillar dimensions are vitally important to producing the desired phase. We also implement this approach in establishing a pixel-based design methodology, where 9 pixel units result in 9 discrete phase levels, and where tiling these units produces the desired metasurface phase maps. Evidencing the flexibility of this approach in generating designed acoustic fields, we implement this in the context of acoustic holography, yielding a range of target fluid-based particle patterning effects. This approach subsequently has the potential to be uniquely suited for microfluidic and/or micromanipulation applications, with utility in acoustic holography, microassembly, tissue engineering, and medical ultrasound.

5. Experimental Section

Calculation of Hologram Plane: The IASA[71,81–83] was used to predict the phase distribution of the hologram plane. Considering that $U(x, y, 0)$ was the acoustic pressure wave of the $z = 0$ plane, its angular spectrum $A(k_x,k_y,0)$ could be obtained via Fourier transform

$$A\left(k_x,k_y,0\right)=\int\int_{-\infty}^{\infty}U\left(x,y,0\right)e^{-j\left(xk_x+yk_y\right)}\mathrm{d}x\mathrm{d}y \tag{3}$$

where k_x and k_y are the wavenumber in x and y, respectively. When $A(k_x,k_y,0)$ propagated to a new plane along the z-axis, the angular spectrum $A(k_x,k_y,z)$ at z was

$$A\left(k_x,k_y,z\right)=A\left(k_x,k_y,0\right)H\left(k_x,k_y,z\right) \tag{4}$$

The transfer function $H(k_x,k_y,z)$ was expressed as

$$H\left(k_x,k_y,z\right)=e^{jz\sqrt{k^2-k_x^2-k_y^2}} \tag{5}$$

where $k = 2\pi/\lambda_m$ is the wavenumber in the medium. The wave function $U(k_x,k_y,z)$ at z could be obtained by inverse Fourier transform of its angular spectrum

$$U(x,y,z) = \frac{1}{4\pi^2}\int\int_{-\infty}^{\infty} A(k_x,k_y,z)\, e^{j(xk_x+yk_y)}\mathrm{d}k_x\mathrm{d}k_y \tag{6}$$

The IASA steps were as follows: 1) the pressure field of the hologram plane was transformed into the angular spectrum (Equation (3)) and propagated to the target plane (Equation (4)), 2) the angular spectrum of the target plane was transformed into the wave function (Equation (6)) and the quality of the obtained pressure field was evaluated (steps exited if quality threshold reached), 3) the amplitude of the target plane was reset using the input image, 4) the angular spectrum of the target plane was obtained and backpropagated to the hologram plane, 5) the hologram plane angular spectrum was transformed into the pressure function, where the pressure functions' phase corresponded to the phase of metasurface units, 6) returning to step 1.

The hologram calculation typically converged in <150 iterations. A spatial cutoff frequency was also introduced to reduce aliasing caused at high spatial frequencies. The cutoff frequency k_c was given as[84]

$$k_c = k\sqrt{\frac{0.5L^2}{0.5L^2 + z^2}} \tag{7}$$

where k is the wavenumber in medium and L is the hologram side length.

Metasurface Fabrication: Metasurfaces were produced on 500 µm-thick 4 in. silicon wafers using conventional photolithography and etching processes. A 28 µm-thick photoresist mask (for etching) was fabricated on the wafer using AZ-40XT positive photoresist (Microchemicals GmbH, Ulm, Germany) according to the manufacturer's instructions. The mask was then hardened at 80 °C for 20 min. The silicon wafer was then etched to the target depth of 260.15 µm by the standard Bosch (deep reactive ion etching, DRIE) process[85] in a DRIE system (Oxford Instruments Plasmalab 100, UK), resulting in a substrate depth height of ≈240 µm. For the purposes of the definition of terms, the metasurface itself has a depth equal to the height of silicon pillar elements, and comprises the silicon pillar/water composite region, where the monolithic silicon substrate depth immediately below this region serves as a support and backing material for the silicon metasurface pillar elements. The phase map that is encoded in the metasurface domain is not a function of the substrate depth, however, and which is dictated in the parameters in Equation (2). A phase delay, however, is introduced between the transducer and the top of the substrate/bottom of the metasurface domain according to $\varphi = L/c\omega$, which for a 240 µm-thick substrate corresponds to ≈70°, though this delay was uniform at the substrate/metasurface boundary and does not impact the phase distribution produced by the metasurface. The effect of substrate height and material on the unit transmission coefficient is further described in the Supporting Information, and the transmission coefficients for different metasurface unit compositions is listed in Table S1 (Supporting Information). While other materials might yield improved transmission coefficients compared to silicon, its combination of high sound speed (yielding lower metasurface thicknesses) and ready ability to etch high-aspect ratio structures to defined depths made this material practical and appropriate for this study.

Acoustic Transducer Fabrication: A 4 in. 128° Y-cut $LiNbO_3$ wafer was subjected to e-beam evaporation for electrode layer deposition of (Cr 25 nm/Al 250 nm). This step was then repeated on the other side of the wafer. Wafers were diced into 1.5 × 1.65 cm chips, with the longer width in 1D permitting the formation of electrical contact on both sides of the transducer. The upper side of the wafer was spin-coated with a protective photoresist layer, followed by acetone, isopropyl alcohol, and deionized water for removing the protective layer.

Experimental Setup: The experimental setup consisted of a polypropylene container (113 mm × 167 mm × 58 mm) with acoustic damping polymer (First Contact, WI, USA) lined on the inside domain of the container and filled with deionized water, as shown in Figure S10 (Supporting Information). The transducer was secured to the bottom of the vessel by polyimide tape and the metasurface hologram was mounted on top of the transducer. The 3D printed acoustic window filled with PDMS particles (see Figure S11 in the Supporting Information for details) was covered with polyethylene terephthalate film at both sides and suspended above the acoustic hologram plane for visualizing the target acoustic field. The 6.9 MHz continuous sine signal generated by the function generator (DG4162, Rigol, Beijing, China) was amplified to 0.8 W by an amplifier (TVA-R5-13A+, Mini Circuits, NY, USA) and connected by a coaxial cable and copper foil tape to actuate the acoustic transducer, where 6.9 MHz corresponded to the first resonant frequency of the transducer. A needle hydrophone probe (200 µm needle hydrophone, Precision Acoustics Ltd., Dorchester, UK) was mounted on a motorized stage (MOXYZ-02-50-50-50, Optics-Focus, Beijing, China) and used to scan the acoustic pressure field. The hydrophone amplifier was connected to a digital oscilloscope (2208B, Picoscope, St Neots, UK), in which a MATLAB script was used to control all instruments and acquire data.

Supporting Information

Supporting Information is available from the Wiley Online Library or from the author.

Acknowledgements

This work was performed in part at the Melbourne Centre for Nanofabrication (MCN) in the Victorian Node of the Australian National Fabrication Facility (ANFF). D.J.C. was the recipient of a Discovery Early Career Researcher Award from the Australian Research Council (DECRA, Grant No. DE200100909), and funding from the National Health and Medical Research Council (Ideas, Grant No. APP2003446).

Open access publishing facilitated by The University of Melbourne, as part of the Wiley - The University of Melbourne agreement via the Council of Australian University Librarians.

Note: Equation (2) was corrected on April 6, 2023, after initial publication online.

Conflict of Interest

The authors declare no conflict of interest.

Data Availability Statement

The data that support the findings of this study are available from the corresponding author upon reasonable request.

Keywords

acoustic holograms, acoustic metasurfaces, metamaterials, micromanipulation

Received: September 1, 2022
Revised: January 13, 2023
Published online: March 6, 2023

---

[1] H.-T. Chen, W. J. Padilla, J. M. O. Zide, A. C. Gossard, A. J. Taylor, R. D. Averitt, *Nature* **2006**, *444*, 597.

[2] G. Zheng, H. Mühlenbernd, M. Kenney, G. Li, T. Zentgraf, S. Zhang, *Nat. Nanotechnol.* **2015**, *10*, 308.
[3] G. Ma, M. Yang, S. Xiao, Z. Yang, P. Sheng, *Nat. Mater.* **2014**, *13*, 873.
[4] L. Huang, S. Zhang, T. Zentgraf, *Nanophotonics* **2018**, *7*, 1169.
[5] S. Wang, P. C. Wu, V.-C. Su, Y.-C. Lai, C. Hung Chu, J.-W. Chen, S.-H. Lu, J. Chen, B. Xu, C.-H. Kuan, T. Li, S. Zhu, D. P. Tsai, *Nat. Commun.* **2017**, *8*, 187.
[6] C. Jung, G. Kim, M. Jeong, J. Jang, Z. Dong, T. Badloe, J. K. W. Yang, J. Rho, *Chem. Rev.* **2021**, *121*, 13013.
[7] S. Yves, R. Fleury, T. Berthelot, M. Fink, F. Lemoult, G. Lerosey, *Nat. Commun.* **2017**, *8*, 16023.
[8] F. Lemoult, N. Kaina, M. Fink, G. Lerosey, *Nat. Phys.* **2013**, *9*, 55.
[9] J. Zhu, J. Christensen, J. Jung, L. Martin-Moreno, X. Yin, L. Fok, X. Zhang, F. J. Garcia-Vidal, *Nat. Phys.* **2011**, *7*, 52.
[10] N. I. Zheludev, Y. S. Kivshar, *Nat. Mater.* **2012**, *11*, 917.
[11] C. M. Watts, X. Liu, W. J. Padilla, *Adv. Mater.* **2012**, *24*, OP98.
[12] C. Meng, P. C. V. Thrane, F. Ding, S. I. Bozhevolnyi, *Nat. Commun.* **2022**, *13*, 2071.
[13] A. H. Dorrah, N. A. Rubin, A. Zaidi, M. Tamagnone, F. Capasso, *Nat. Photonics* **2021**, *15*, 287.
[14] M. Xu, P. V. S. Lee, D. J. Collins, *Lab Chip* **2022**, *22*, 90.
[15] Y. Fu, Y. Tian, X. Li, S. Yang, Y. Liu, Y. Xu, M. Lu, *Phys. Rev. Lett.* **2022**, *128*, 104501.
[16] X.-F. Zhu, S.-K. Lau, *J. Appl. Phys.* **2019**, *126*, 224504.
[17] Z. Xu, L. Qin, W. Xu, S. Fang, J. Wang, *Sci. Rep.* **2021**, *11*, 7619.
[18] J. Rong, W. Ye, S. Zhang, Y. Liu, *Adv. Funct. Mater.* **2020**, *30*, 2005285.
[19] H. Zhu, F. Semperlotti, *Phys. Rev. Lett.* **2016**, *117*, 034302.
[20] B. Assouar, B. Liang, Y. Wu, Y. Li, J.-C. Cheng, Y. Jing, *Nat. Rev. Mater.* **2018**, *3*, 460.
[21] N. Yu, P. Genevet, M. A. Kats, F. Aieta, J.-P. Tetienne, F. Capasso, Z. Gaburro, *Science* **2011**, *334*, 333.
[22] X. Wang, D. Mao, Y. Li, *Sci. Rep.* **2017**, *7*, 11604.
[23] S.-W. Fan, S.-D. Zhao, L. Cao, Y. Zhu, A.-L. Chen, Y.-F. Wang, K. Donda, Y.-S. Wang, B. Assouar, *Phys. Rev. B* **2020**, *101*, 024104.
[24] H.-T. Zhou, S.-W. Fan, X.-S. Li, W.-X. Fu, Y.-F. Wang, Y.-S. Wang, *Smart Mater. Struct.* **2020**, *29*, 065016.
[25] Z. Chen, F. Yan, M. Negahban, Z. Li, *J. Appl. Phys.* **2021**, *130*, 125304.
[26] K. Donda, Y. Zhu, S.-W. Fan, L. Cao, Y. Li, B. Assouar, *Appl. Phys. Lett.* **2019**, *115*, 173506.
[27] J. Guo, X. Zhang, Y. Fang, Z. Jiang, *Appl. Phys. Lett.* **2020**, *117*, 221902.
[28] H. Ryoo, W. Jeon, *J. Appl. Phys.* **2018**, *123*, 115110.
[29] J. Zhao, H. Ye, K. Huang, Z. N. Chen, B. Li, C.-W. Qiu, *Sci. Rep.* **2015**, *4*, 6257.
[30] D.-C. Chen, X.-F. Zhu, Q. Wei, D.-J. Wu, X.-J. Liu, *J. Appl. Phys.* **2018**, *123*, 044503.
[31] J. Xia, X. Zhang, H. Sun, S. Yuan, J. Qian, Y. Ge, *Phys. Rev. Appl.* **2018**, *10*, 014016.
[32] K. Gong, X. Wang, H. Ouyang, J. Mo, *J. Phys. D: Appl. Phys.* **2019**, *52*, 385303.
[33] S. Tang, B. Ren, Y. Feng, J. Song, Y. Jiang, *J. Appl. Phys.* **2021**, *129*, 155307.
[34] X.-L. Wang, J. Yang, B. Liang, J.-C. Cheng, *Appl. Phys. Express* **2020**, *13*, 014002.
[35] A. Melnikov, S. Köble, S. Schweiger, Y. K. Chiang, S. Marburg, D. A. Powell, *Adv. Sci.* **2022**, *9*, 2200990.
[36] W. Wang, Y. Xie, B.-I. Popa, S. A. Cummer, *J. Appl. Phys.* **2016**, *120*, 195103.
[37] Y. Li, B. Liang, Z. Gu, X. Zou, J. Cheng, *Sci. Rep.* **2013**, *3*, 2546.
[38] A. Díaz-Rubio, S. A. Tretyakov, *Phys. Rev. B* **2017**, *96*, 125409.
[39] Y. Li, X. Jiang, B. Liang, J. Cheng, L. Zhang, *Phys. Rev. Appl.* **2015**, *4*, 024003.
[40] Y. Zhu, B. Assouar, *Phys. Rev. Mater.* **2019**, *3*, 045201.
[41] J. Zhang, Y. Tian, Y. Cheng, X. Liu, *Appl. Phys. Lett.* **2020**, *116*, 030501.
[42] S.-W. Fan, Y. Zhu, L. Cao, Y.-F. Wang, A.-L. Chen, A. Merkel, Y.-S. Wang, B. Assouar, *Smart Mater. Struct.* **2020**, *29*, 105038.
[43] J. Li, A. Song, S. A. Cummer, *Phys. Rev. Appl.* **2020**, *14*, 044012.
[44] G. Su, Y. Liu, *Appl. Phys. Lett.* **2020**, *117*, 221901.
[45] H. Zou, P. Li, P. Peng, *Phys. Lett. A* **2020**, *384*, 126151.
[46] Y. Tang, Y. Zhang, B. Xie, H. Cheng, J. Tian, S. Chen, *Phys. Rev. Appl.* **2022**, *17*, 044027.
[47] B. Xie, K. Tang, H. Cheng, Z. Liu, S. Chen, J. Tian, *Adv. Mater.* **2017**, *29*, 1603507.
[48] Y. Zhu, K. Donda, S. Fan, L. Cao, B. Assouar, *Appl. Phys. Express* **2019**, *12*, 114002.
[49] R. Ghaffarivardavagh, J. Nikolajczyk, R. G. Holt, S. Anderson, X. Zhang, *Nat. Commun.* **2018**, *9*, 1349.
[50] H. Ryoo, W. Jeon, *Appl. Phys. Lett.* **2018**, *113*, 121903.
[51] S.-D. Zhao, A.-L. Chen, Y.-S. Wang, C. Zhang, *Phys. Rev. Appl.* **2018**, *10*, 054066.
[52] J. Lan, Y. Li, Y. Xu, X. Liu, *Sci. Rep.* **2017**, *7*, 10587.
[53] S. Tang, C. Lü, J.-L. Wu, J. Song, Y. Jiang, *Appl. Acoust.* **2022**, *194*, 108786.
[54] Y. Zhu, B. Assouar, *Phys. Rev. B* **2019**, *99*, 174109.
[55] N. J. Gerard, H. Cui, C. Shen, Y. Xie, S. Cummer, X. Zheng, Y. Jing, *Appl. Phys. Lett.* **2019**, *114*, 231902.
[56] H. Ryoo, W. Jeon, *Int. J. Mech. Sci.* **2022**, *229*, 107508.
[57] J. Qian, Y. Wang, S. Yuan, H. Sun, X. Liu, *Appl. Phys. Express* **2019**, *12*, 094001.
[58] X.-S. Li, Y.-F. Wang, A.-L. Chen, Y.-S. Wang, *Sci. Rep.* **2019**, *9*, 15856.
[59] G. Liao, C. Luan, Z. Wang, J. Liu, X. Yao, J. Fu, *Adv. Mater. Technol.* **2021**, *6*, 2000787.
[60] S. Kumar, H. Pueh Lee, *Int. J. Appl. Mech.* **2019**, *11*, 1950081.
[61] B. Liu, W. Zhao, Y. Jiang, *Sci. Rep.* **2016**, *6*, 38314.
[62] C. Ding, X. Zhao, H. Chen, S. Zhai, F. Shen, *Appl. Phys. A* **2015**, *120*, 487.
[63] B. Liu, Y. Jiang, *Appl. Phys. Lett.* **2018**, *112*, 173503.
[64] J. Lan, X. Zhang, X. Liu, Y. Li, *Sci. Rep.* **2018**, *8*, 14171.
[65] L.-X. Han, Y.-W. Yao, X. Zhang, F.-G. Wu, H.-F. Dong, Z.-F. Mu, J. Li, *Phys. Lett. A* **2018**, *382*, 357.
[66] C. Zhang, W. K. Cao, L. T. Wu, J. C. Ke, Y. Jing, T. J. Cui, Q. Cheng, *Appl. Phys. Lett.* **2021**, *118*, 133502.
[67] H. Tang, Z. Hao, J. Zang, *J. Appl. Phys.* **2019**, *125*, 154901.
[68] K. Kolesnik, M. Xu, P. V. S. Lee, V. Rajagopal, D. J. Collins, *Lab Chip* **2021**, *21*, 2837.
[69] J. Kim, S. Kasoji, P. G. Durham, P. A. Dayton, *Appl. Phys. Lett.* **2021**, *118*, 051902.
[70] S. Jiménez-Gambín, N. Jiménez, J. M. Benlloch, F. Camarena, *Sci. Rep.* **2019**, *9*, 20104.
[71] K. Melde, A. G. Mark, T. Qiu, P. Fischer, *Nature* **2016**, *537*, 518.
[72] J. G. Berryman, *J. Acoust. Soc. Am.* **1980**, *68*, 1820.
[73] J. Mei, Z. Liu, W. Wen, P. Sheng, *Phys. Rev. Lett.* **2006**, *96*, 024301.
[74] Z. Hou, X. Fang, Y. Li, B. Assouar, *Phys. Rev. Appl.* **2019**, *12*, 034021.
[75] Y. Zhu, A. Merkel, K. Donda, S. Fan, L. Cao, B. Assouar, *Phys. Rev. B* **2021**, *103*, 064102.
[76] L. Quan, A. Alù, *Phys. Rev. Appl.* **2019**, *11*, 054077.
[77] H. Ding, X. Fang, B. Jia, N. Wang, Q. Cheng, Y. Li, *Phys. Rev. Appl.* **2021**, *16*, 064035.
[78] M. D. Brown, *Appl. Phys. Lett.* **2019**, *115*, 053701.
[79] M. D. Brown, B. T. Cox, B. E. Treeby, *Appl. Phys. Lett.* **2020**, *116*, 261901.
[80] Z. Ma, K. Melde, A. G. Athanassiadis, M. Schau, H. Richter, T. Qiu, P. Fischer, *Nat. Commun.* **2020**, *11*, 4537.
[81] D.-L. Liu, R. C. Waag, *IEEE Trans. Sonics Ultrason.* **1997**, *44*, 1.
[82] S. Mellin, G. Nordin, *Opt. Express* **2001**, *8*, 705.
[83] K. Matsushima, T. Shimobaba, *Opt. Express* **2009**, *17*, 19662.
[84] X. Zeng, R. J. McGough, *J. Acoust. Soc. Am.* **2008**, *123*, 68.
[85] F. Marty, L. Rousseau, B. Saadany, B. Mercier, O. Français, Y. Mita, T. Bourouina, *Microelectronics J.* **2005**, *36*, 673.